Rarefied gas flows in complex microfluidic 3D-structures fabricated via additive manufacturing

Franz Schweizer, Klaus Bade, Lucien Baldas, Samuel Bergdolt, Stéphane Colin, Celine Deutschbein, Stefan Hengsbach, Jan Korvink, Marcos Rojas-Cárdenas, Jürgen Brandner

Vacuum 238 (2025) 114213

Contents lists available at ScienceDirect

Vacuum

journal homepage: www.elsevier.com/locate/vacuum

Rarefied gas flows in complex microfluidic 3D-structures fabricated via additive manufacturing

Franz Schweizer [a,b], Klaus Bade [b,c], Lucien Baldas [a], Samuel Bergdolt [b,c], Stéphane Colin [a], Celine Deutschbein [b,c], Stefan Hengsbach [b,c], Jan G. Korvink [b], Marcos Rojas-Cárdenas [a,*], Jürgen J. Brandner [b,c]

[a] Institut Clément Ader (ICA), Université de Toulouse CNRS, INSA, ISAE-SUPAERO, IMT Mines-Albi, Toulouse, France
[b] Institute of Microstructure Technology (IMT), Karlsruhe Institute of Technology, Eggenstein-Leopoldshafen, Germany
[c] Karlsruhe Nano Micro Facility (KNMFi), Karlsruhe Institute of Technology, Eggenstein-Leopoldshafen, Germany

ARTICLE INFO

Keywords:
Microfluidics
Rarefied gas flows
3D micro-structures
Tapered microchannels
Additive-manufacturing
Two photon polymerization

ABSTRACT

In this work, two-photon-polymerization (TPP) is introduced as a method for manufacturing three-dimensional devices for rarefied gas flow applications. The novel 3D manufacturing capabilities of TPP are demonstrated by the fabrication of a microfluidic structure that consists of a circular micro-tube with a varying radius (tapered channel). The micro-tube has interesting features, such as a conical structure with one order of magnitude difference between minimum and maximum radii, that is 14 μm and 215 μm, respectively, and a very high aspect ratio, that is defined as the length over the minimum radius, of 72.3. To our knowledge, this is the first time that such a geometrical configuration has been successfully tested for rarefied gas flow applications. It supports the suitability of the presented fabrication method for further 3D new-generation applications in the field. The geometrical characteristics of the device were measured by μ-tomography and subsequently analyzed allowing the assessment of the geometrical precision of the fabrication method. From a fluid dynamics perspective, the device was tested by imposing pressure-driven gas flows in the converging and diverging directions of the structure for a wide range of rarefaction. The flow parameters linked to the structure, such as mass flow rates and conductances, were obtained experimentally using the constant volume technique. The experimental results were compared to numerical simulations obtained via Computational Fluid Dynamics solving the Navier–Stokes equation in the slip and hydrodynamic flow regimes. The experimental vs. numerical comparison showed good agreement within geometrical uncertainty.

1. Introduction

The characterization of gas flows in microdevices of controlled geometry is of great importance for the development of micro-electro-mechanical-systems (MEMS). Applications include fluid delivery in lab-on-a-chip, gas chromatography, flow sensors and gas separation devices [1–4].

Gas flows can be considered as rarefied if the mean free path λ_{fp} of the gas molecules is in the same order of magnitude as the characteristic length L of the flow. The degree of rarefaction is therefore often quantified using the Knudsen number $Kn = \lambda_{fp}/L$. As the mean free path of a gas is increasing with decreasing absolute pressure, rarefied gas flows are found at low absolute pressures or in devices with characteristic lengths in the micrometer range. Rarefied gas flows are characterized by a low ratio of intermolecular collisions in respect to gas-surface collisions, which leads to a non-equilibrium thermodynamic state in the gas, thereby making continuum flow modeling approaches non-applicable. Rarefied flows can be categorized into the slip flow regime for $0.01 \leq Kn \leq 0.1$ (low rarefaction), the transitional flow regime for $0.1 \leq Kn \leq 10$ (moderate rarefaction) and the molecular flow regime for $10 \leq Kn$ (high rarefaction) [5].

Nowadays, concerning the design and manufacturing of microfluidic devices containing gas flows, the ability of fabricating precise micro-scale geometries remains one of the main challenges. To date, experimental studies reported in the literature describe microchannels or microtubes obtained using one of the following: (i) Mechanical micro-milling of polymers and metals [6,7]; (ii) Planar-lithographically-patterned processes such as dry-film lamination resulting in a final polymer structure [8], wet-etching [9–11], and deep reactive ion etching of bulk silicon [12–14], or even etching of silicon oxide layers [15–17] to fabricate channels of nanometer dimensions; (iii) Commercially

* Corresponding author.
E-mail address: marcos.rojas@insa-toulouse.fr (M. Rojas-Cárdenas).

https://doi.org/10.1016/j.vacuum.2025.114213
Received 18 October 2024; Received in revised form 28 February 2025; Accepted 3 March 2025
Available online 15 March 2025

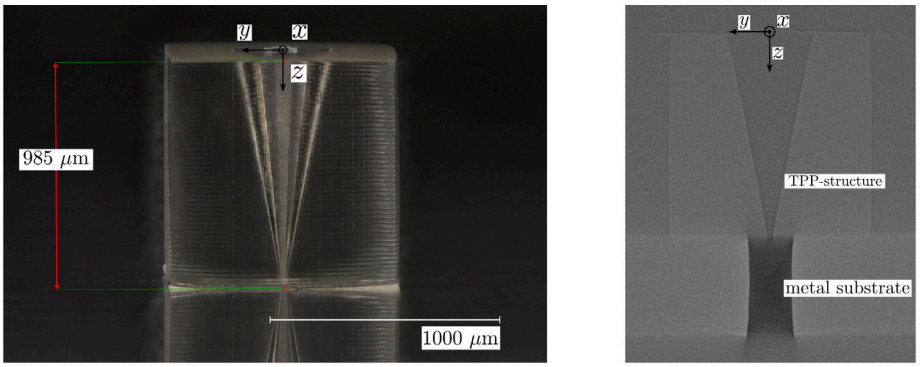

(a) Microscopy image. (b) Tomography image.

Fig. 1. Tapered channel sample generated on a metal substrate with a hole.

available micro-capillaries fabricated in metal [18–20] or silica [21–23], and commercially available porous media in the sub-μm range such as silica aerogels [24], ceramics [25], and cellulose [26].

However, it is important to point out that these fabrication techniques have strong limitations. Micro-milling and standard lithographic processes are limited to 2.5D geometries within the plane of the substrate, making it difficult to manufacture circular cross-section channels with high aspect ratio or three-dimensional geometries. Furthermore, these processes require closing of the fabricated channels using a top cover, adding an extra process step, typically done by anodic bonding with a silicon or glass cover wafer. Commercially available long tubes at the micrometer scale are limited to capillaries with diameters greater than 80 μm, owing to the tube drawing process. Moreover, these elements are extremely difficult to integrate in a complex architecture system at the micro-scale. Finally, commercially available porous media, which were employed for practical applications such as Knudsen pumps, are not suitable for the precise validation of numerical flow models because of the random nature of their internal geometry. The necessity of having a statistical characterization of the geometry creates great difficulties when defining the flow domain.

In light of these limitations, two-photon-polymerization (TPP) offers an extraordinary potential for developing 3D new generation microfluidic devices. Until now, TPP was explored as a fabrication method in the area of liquid microfluidics, such as for the manufacturing of master structures by TPP for PDMS molding of micromixers [27] and the direct printing of suspended filtration systems inside a microchannel [28]. Thereby showcasing the potential of combining TPP and other common patterning methods in microfluidics. Also, highly compliant structures fabricated by TPP have been utilized for acoustically actuated microrotors [29] and pumps [30].

Recently, our group has demonstrated that TPP can be successfully used for manufacturing of microfluidic structures dedicated to rarefied gas flows [31]. As an extension of our previous work, where we tested constant diameter micro-tubes [31], we introduce and showcase the potential of TPP based micro 3D-printing for the fabrication of complex micro-devices suitable for rarefied gas flows. Using this fabrication technique, it was thus possible to experimentally investigate rarefied gas flows in a circular microtube of varying radius (tapered channel). Tapered structures are of great interest, since they have potential applications in micro-thrusters [32] and Knudsen pumps [33]. From a numerical point of view, gas flows through tapered channel configurations have been extensively studied in the literature by applying modeling approaches of different complexity, ranging from 1D-models utilizing kinetic and continuum theory [34,35] to 2D- and 3D-modeling utilizing the Discrete Velocity and Direct Simulation Monte-Carlo methods [36–40]. To our knowledge, the only work presenting both experimental and numerical results for tapered channels corresponds to the work of [7,32], which were realized only for planar tapered structures.

We propose via this work experimental and numerical results of rarefied gas flowing in a micro-tapered-tube structure. A major achievement of this work is the manufacturing process of a 3D shaped micro-tapered-tube obtained via TPP. The micro-structure has very interesting features, such as a conical structure with one order of magnitude difference between minimum (14 μm) and maximum radii (215 μm), and very high aspect ratio, that is length over minimum radius of 72.3. To our knowledge, due to the complexity related to fabricating such channels, this is the first experimental and numerical characterization of this type of flows that can be found in the literature.

2. Fabrication by two-photon-polymerization

Two-photon-polymerization allows the creation of 3D structures starting from a photosensitive viscous fluid which is locally polymerized by a high-energy laser moving in space. More specifically, a pulsed laser is focused in order to excite the photo-starter molecule which in turn starts a polymerization reaction. The resin material solidifies in a prescribed geometry. The focal point of the laser is moved within the field of view (FOV) of the objective using a galvo-scan unit. The geometry is built up from ellipsoid voxels. Similar to most additive manufacturing processes, the method imposes very little restrictions on possible designs. Opposing to the one-photon-polymerization process, in TPP the photo-starter can only reach its excited state if two photons are absorbed at the same location within a very limited time frame. The probability of two-photon-absorption is proportional to the light intensity squared, thus only a small area in the center of the focal point reaches the intensity threshold to start the curing of the liquid resin. Therefore, the structure size is not directly limited by the dimensions of the focal point of the laser. Because of this highly localized induction of the photochemical reaction, sizes of features down to 100 nm are possible [41].

TPP allows for the fabrication of high-precision polymer structures directly from a common stereolithography file which can be created in a straight-forward manner via computer-aided design software. Thus, there is no need for multiple process steps or the fabrication of masks which is typically required in lithography based fabrication methods. Manufacturing cycle times can therefore be reduced, due to the reduced complexity of the process. Furthermore, even if the outer dimensions of the manufactured structures are limited by the FOV of the objective used, larger structures can be fabricated by moving the stage supporting the sample and stitching interfaces between different printed blocks. However, this solution creates problems with respect to geometrical defects at the interface. Large area structuring of substrates using TPP is thus still challenging. Moreover, increasing manufactured volumes implies higher manufacturing times due to the sequential nature of the process.

In this work, we have extended the limits of usage of the TPP manufacturing technique in terms of dimensions and geometry achieved:

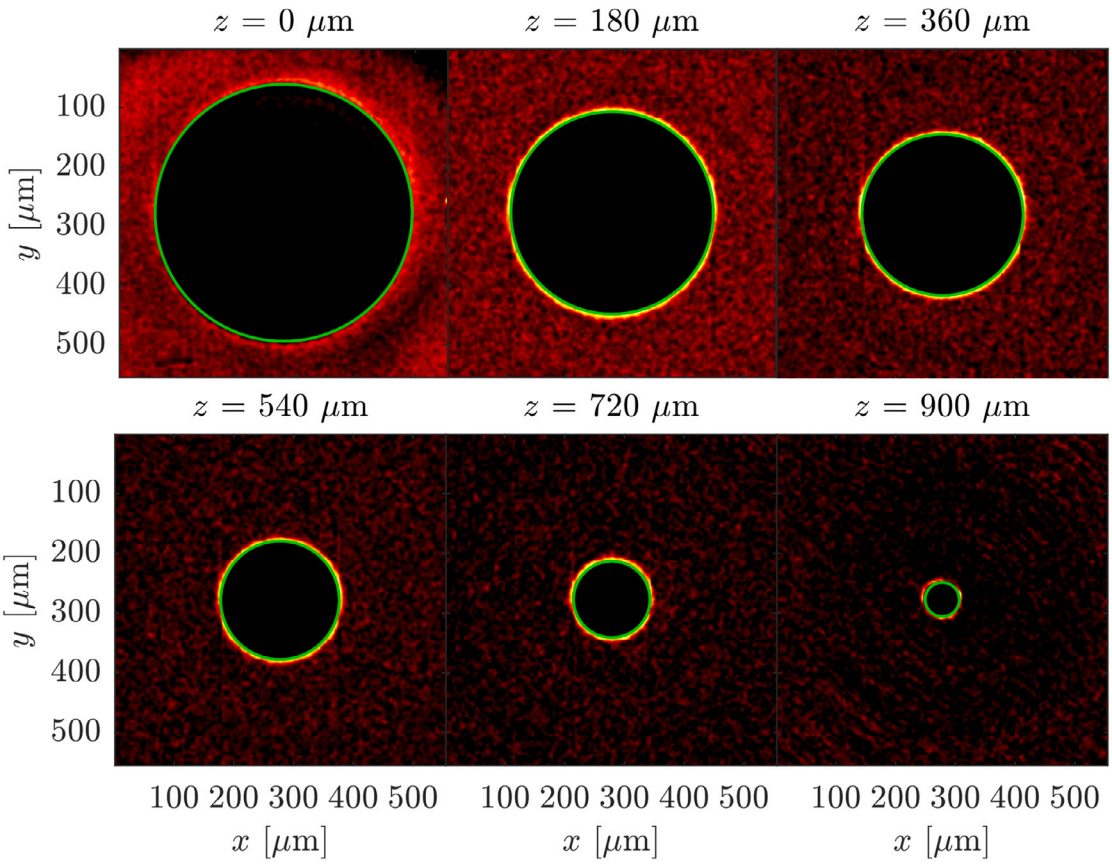

Fig. 2. Images of channel cross-sections, and detected circular perimeter (green).

the three-dimensional device has a very high aspect ratio and a cross-section size varying by one order of magnitude along the device. As depicted in Fig. 1, the conical channel was created inside a cube of approximately 1 mm^3. The structure was deposited over an aluminum substrate of dimensions 25 mm × 25 mm × 0.5 mm. The substrate includes a milled circular orifice of approximately 200 μm in diameter that allows connecting the tapered channel to the other side of the substrate. It can be seen from these images that the adhesion between polymer and metal substrate is sufficient to ensure a leak-tight interface. This is an extremely important feature for avoiding gas leakages between the printed structure and the rest of the experimental setup, as the metal substrate also has the function of hydraulic connectivity. The manufacturing was accomplished with a Photonic Professional GT 2 system (Nanoscribe GmbH). The main components of this device are a pulsed femtosecond-laser combined with focusing optics and a sample holder. A 10× magnification objective with a 0.3 numerical aperture was used. The sample was fabricated within one FOV of the objective, corresponding to outer dimensions of 1 × 1 × 1mm^3. The fabrication of millimeter sized structures in one FOV represents a further extension of the capabilities of the process compared to earlier works [31]. It showcases the potential manufacturing of geometries with feature sizes ranging multiple orders of magnitude. The laser was operated with a 80 MHz pulse frequency, 100 fs pulse duration and an average power of 80%. The structure was created by sequentially polymerizing the photoresist (IP-Q Nanoscribe GmbH) with a scanning speed of 50 mm/s. With these fabrication parameters the voxel length is approximately 25.4 μm and the voxel diameter 1.6 μm [42]. The total printing time for this sample was 50 min (min). For manufacturing purposes, the geometry was decomposed into layers with a slicing height of 5 μm. These layers are, in turn, discretized with a lateral hatching size of 1 μm. Taking into account the estimated voxel size and the slicing and hatching distances, the arithmetic roughness (R_a) of the surface inside of the tapered section of the sample is approximately 133 nm [43]. Once the writing process was completed, the uncured resin was removed using a two-step development process consisting of a propylene glycol methylether acetate (PGMEA) bath for 2 h (h), followed by rinsing for 2 min. The process was repeated with fresh PGMEA for a total development time of approximately 14 h. Finally the sample was dried for 30 min at 7 °C. It is important to point out that the polymer shrinks during the development process. This shrinkage results in geometrical errors and residual stresses in the material. The shrinkage of the structure during the development process makes in-depth characterization of the internal geometry necessary. To capture these geometric deviations, the sample was analyzed with the help of a μ-tomograph.

3. Dimensional characterization of the sample

For characterization purposes a coordinate system originating at the center of the larger opening of the tapered channel is introduced (Fig. 1), with the z-direction being oriented along the axis of the tapered channel. The internal geometry of the sample was analyzed with a EasyTom XL tomograph (RX Solutions). Due to the outer dimensions of the substrate and the measurement equipment used, the resolution was limited. The obtained tomograms had an isotropic voxel size of dx = 2.77 μm. Images were obtained for the three planes of the structure, however for the purposes of this analysis, and due to the axisymmetric nature of the sample, only the cross-sectional planes (x-y) and the longitudinal planes (y-z) were analyzed. The longitudinal y-z-plane images were used to measure the length and radius of the sample. The y-z-slice closest to the rotational axis (Fig. 1(b)) was used, in combination with an edge detection filter, to extract the radius distribution and length of the channel structure. The sliced x-y-images perpendicular to the z-axis were analyzed to verify the radius

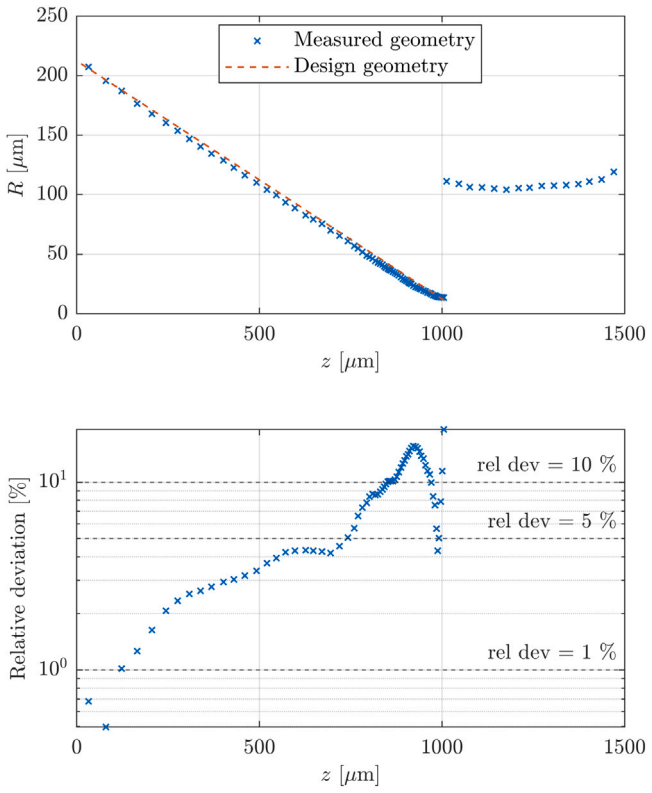

Fig. 3. Relative deviation of real and design geometries.

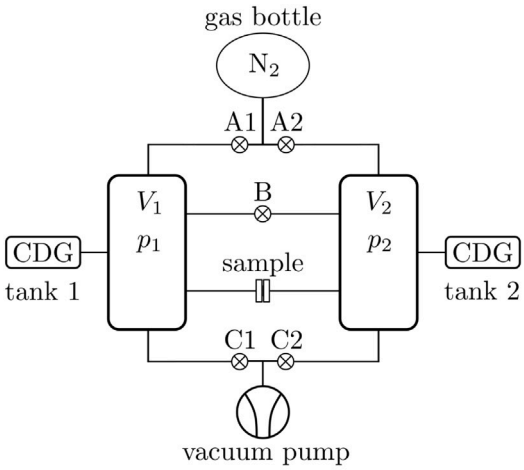

(a) Schematic diagram of the experimental setup.

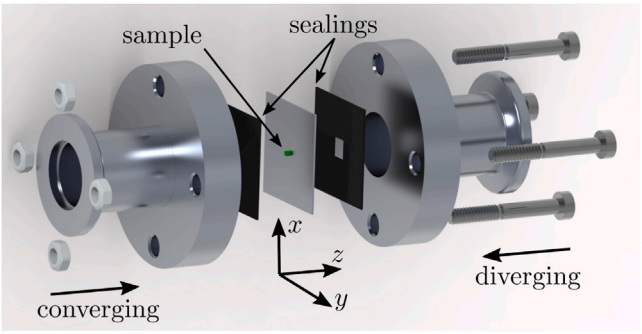

(b) Casing assembly model.

Fig. 4. Experimental setup.

measurements and evaluate the circularity of the cross-section along the z-axis of the channel. The analysis was realized by using a routine based on the circular Hough transform (Matlab R2022b, MathWorks Inc.). A selection of x-y tomography images including the detected cross-sections (green) is shown in Fig. 2. The channel cross-sections show excellent circularity throughout the whole length of the channel. Judging from the circularity of the cross-sections, possible shrinkage effects did not alter the circular shape of fabricated structures. The images depicted in Fig. 2 show the same dimensional scale in order to portray the great difference in terms of cross-section dimension along the axis. However, if the image is zoomed around the cross-section of interest, the same precision of fabrication is found at each z-value.

The central slice in the y-z-plane was analyzed as previously described, yielding the radius distribution as a function of the z-axis of the channel. The TPP-printed structure of the tapered channel was appropriately defined along its full length L, i.e., in a z-range of [0,1012] μm, while the physical domain occupied by the circular orifice in the metal substrate was located in the [1012,1470] μm z-range (Fig. 3 top). The measurements suggest that the radius of the channel is varying from approximately $R = 215$ μm at $z = 0$ to $R = 14$ μm at $z = L$. The uncertainty related to this measurement was estimated via a propagation of uncertainty principle. The spatial resolution of the measurement depends on the voxel size provided by the tomography measurement, thus, in one image it was possible to define the position x with an uncertainty $\epsilon = \pm \mathrm{d}x/2$, where $\mathrm{d}x$ is the voxel length in the x-direction. Since a distance is calculated through the definition of two independent positions, it was also possible to define the radius uncertainty via a propagation of uncertainty principle, as $\Delta R = \pm\sqrt{2}\epsilon$, i.e., approximately ±1.96 μm.

The relative deviation between the fabricated geometry, measured via μ-tomography, and the originally designed geometry, i.e., the input geometry for fabrication, is depicted in Fig. 3 bottom. The radius distribution in the entrance and central region $z \leq 552$ μm of the channel shows a linear distribution and a relative deviation of less than 5% from the designed geometry. The largest deviations of the TPP-sample from the design geometry can be seen at the outlet ($z = 1012$ μm) of the tapered channel, where the radius of the channel is at its minimum ($R = 14$ μm), and here only the μ-tomography measurement uncertainty alone corresponds to almost 15% of the radius value.

The deviation from the design geometry at the extremity of the channel can be explained by the shrinkage of the photoresist during curing and development. A relative shrinkage causes the largest displacements at the extremities of the structure, which corresponds to the outlet section. The large relative deviation at the outlet of the tapered channel is possibly caused by the slender nature of the polymer structure protruding over the orifice in the substrate. The amount of shrinkage is highly dependent on the geometry of the structure, the exposure parameters, and the specific resist used. This phenomenon was also observed in our previous study [31].

The optical characterization showed the potential of TPP to create precise geometries with structure sizes down to tens of μm. Nevertheless, the shrinkage of the photoresist during development is not negligible, making a thorough characterization of the geometry necessary.

4. Fluidic characterization of the sample

The sample was characterized experimentally and numerically with gas flows corresponding to a wide range of gas rarefaction conditions. Pressure driven flows were imposed along the converging and diverging directions of the sample in order to test its capacity to channel such flows effectively. The sample was characterized in terms of conductance as a function of a wide range of nominal pressures. Within this experimental campaign, it was also possible to prove that the sample and the

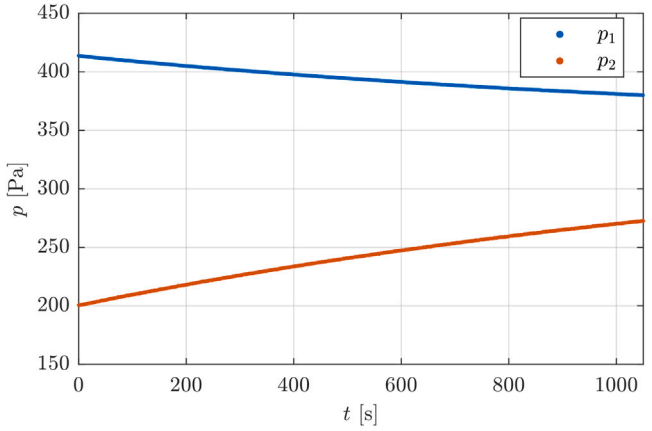

Fig. 5. Example of pressure evolution in tanks 1 and 2 with time.

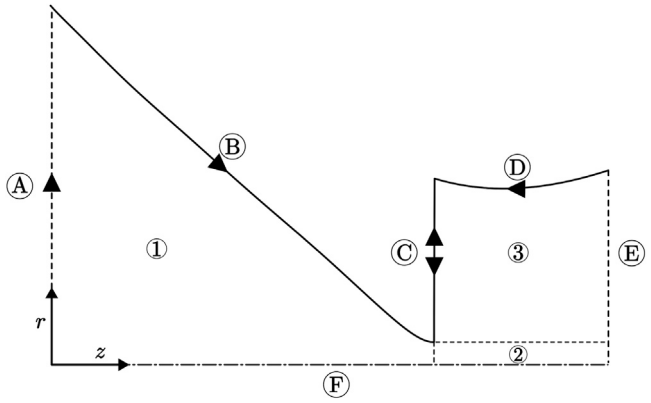

Fig. 6. Illustration of the flow domain [①,②,③] and boundaries [Ⓐ-Ⓕ]. The r- and z-axis are not in the same scale, for reference the nozzle radius at $z = 1012$ μm is $R_L = 14$ μm.

fabrication process were of a very robust nature, since the sample did not detach from the substrate and did not deform under the vacuum conditions tested and the pressure differences imposed.

4.1. Experimental characterization

The experimental campaign consisted of measuring mass flow rates of pressure driven flows in the tapered channel sample via the constant volume technique. The methodology of the constant volume technique consists in relating, inside a constant volume, pressure variations with time to mass variations induced by the gas flowing through the sample. This well known indirect measurement technique allows high precision measurements even for very low mass flow rates [18,31,44–51].

The experimental setup consisted of two tanks, with volumes $V_1 = 162.3$ ml and $V_2 = 86.0$ ml, which were connected by the tapered channel (Fig. 4(a)). The pressure in the two volumes could be regulated by means of an external tank containing nitrogen at high pressure, and a vacuum pump utilizing the valves A1, A2, B, C1, and C2. The pressures p_1 and p_2 in the volumes were monitored using two absolute capacitance diaphragm gauges (CDG) with full ranges of 1333 Pa or 13330 Pa, depending on the mean pressure of the experiment. The measurement accuracy of the used gauges was 0.2% of the reading.

The aluminum substrate supporting the tapered channel sample (green) was clamped inside a casing (Fig. 4(b)). Inside the casing, two rubber seals were used to prevent leakages between the aluminum substrate and the atmosphere.

The experiments were performed by imposing an initial pressure difference between inlet and outlet of the sample, i.e., in tank 1 and tank 2, and then monitoring the pressure variation with time in both tanks. Fig. 5 shows the pressure evolution of a selected experiment. Both converging and diverging flows were tested in the sample. Converging flow relates to a flow directed from the larger cross-section towards the smaller cross-section, which is located respectively at the inlet at $z = 0$, $R_0 = 215$ μm and at the outlet at $z = L$, $R_L = 14$ μm, while diverging flow relates to a flow in the opposite direction. As depicted in Fig. 4(a), tanks 1 and 2 were simultaneously connected to both the high pressure tank and the vacuum pump. This configuration allowed the creation of a $p_1 > p_2$ initial condition for converging flows, and a $p_2 > p_1$ initial condition for diverging flows.

By monitoring the pressure variation with time in both tanks, and by employing the ideal gas law, for negligible fluctuations of temperature, the mass flowrate entering tank i $\dot{m}_i$ could be calculated as

$$\dot{m}_i = \frac{V_i}{R_g T}\frac{\mathrm{d}p_i}{\mathrm{d}t}. \tag{1}$$

V_i, T, p_i, R_g, t being the volume, temperature, pressure of the reservoir, specific gas constant, and time, respectively. The experiment was conducted in a temperature controlled room ($T = 293.15\mathrm{K} \pm 0.5\mathrm{K}$), which was enough to define the temperature of both tanks as the ambient temperature and consider the experiment as isothermal. For this method, the uncertainty in the mass flow measurements was determined to be on the order of 3%. The uncertainty on the mass flow measurement was obtained through the principle of propagation of uncertainties, taking into account the uncertainties on the pressure, temperature and volume measurements [18]. Experiments were performed over a wide range of nominal pressures from 0.1 to 12.5 kPa. This pressure range allowed an experimental characterization over a range of rarefaction conditions, including the transition, slip and hydrodynamic regimes. All pressure combinations were tested for both converging and diverging flow directions. Each experiment was defined by the level of rarefaction of the flow, which was calculated via the Knudsen number Kn_m:

$$Kn_m = k_2 \frac{\mu\sqrt{R_g T}}{p_m R_L} \tag{2}$$

where μ is the dynamic gas viscosity at ambient temperature, $p_m = \frac{p_1+p_2}{2}$ is the mean pressure, R_L is the radius at the nozzle and k_2 is a factor corresponding to the choice of intermolecular model. In this case the variable hard-sphere model is chosen for nitrogen [5]. The complete values of the initially applied pressures at the inlet and outlet of the channel, and the corresponding mean Knudsen number, are specified in Table A.1 (Appendix).

4.2. Numerical modeling

Owing to the complex flow geometry, consisting of either a converging or diverging structure with a sudden expansion or contraction, a computational fluid dynamics (CFD) 2D axissymmetric modeling approach was preferred to kinetic theory models. The CFD modeling was based on solving the Navier–Stokes-Fourier equations with velocity slip conditions at the wall, in order to extend the modeling application range from hydrodynamic to slip regime. Nitrogen was modeled as a Newtonian fluid and ideal gas. Following [52], the velocity boundary conditions were implemented via the rarefied flow module of Comsol Multiphysics 6.1 (COMSOL AB) as

$$\boldsymbol{u} - \boldsymbol{u}_w = \sigma_s \frac{l}{\mu}\left(\boldsymbol{\tau}\boldsymbol{n} - \left(\left(\boldsymbol{n}^{\mathrm{T}}\boldsymbol{\tau}\boldsymbol{n}\right)\boldsymbol{n}\right)\right), \tag{3}$$

$\boldsymbol{u}$, $\boldsymbol{u}_w$, σ_s, $l = \frac{\mu\sqrt{2R_g T}}{p}$, $\boldsymbol{\tau}$, $\boldsymbol{n}$ being the velocity of the fluid, the velocity of the wall, the viscous slip coefficient, the equivalent mean free path, the shear stress tensor, and the normal unit vector of the boundary. This implementation of the slip boundary condition includes possible contributions to the slip velocity caused by the curvature of the bounding wall. According to the practical guidelines in [53], $\sigma_s = 1$ was chosen for the calculations, which corresponds to a fully diffuse surface.

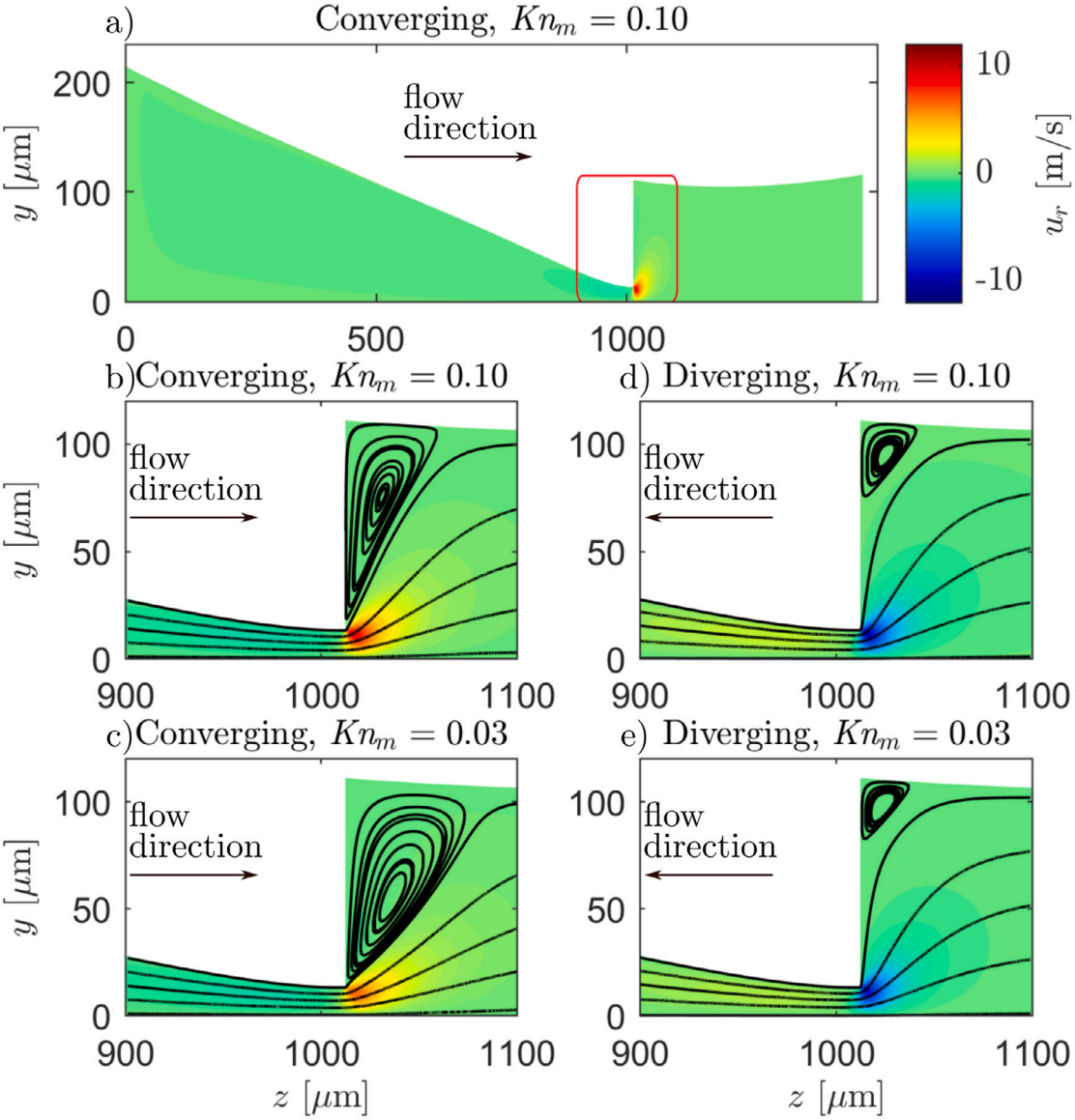

Fig. 7. Radial velocity u_r contours (top) and streamlines in both flow directions, and for two different levels of rarefaction.

The numerical flow domain was generated by using the dimensions of the channel measured via μ-tomography. With this approach, the geometrical defects originating from the fabrication process were taken into account in the simulations. A schematic of the flow domain is shown in Fig. 6. In order to smoothen the raw tomography measurement data, polynomials of different orders were fitted to both the channel section and orifice section of the channel assembly. To account for the higher shrinkage in the exit area of the tapered channel, a high order polynomial was chosen. The piecewise radius function is:

$$R(z) = \begin{cases} \sum_{i=0}^{10} a_i z^i, 0\ \mu\text{m} \le z \le 1012\ \mu\text{m} \\ \sum_{j=0}^{3} b_j z^j, 1012\ \mu\text{m} \le z \le 1470\ \mu\text{m} \end{cases} \quad (4)$$

Table 1 lists the values of the coefficients of the function, which were obtained using a least-squares approach. Owing to the high sensitivity of the simulation results to the domain size, the coefficients are given with the number of significant figures needed to ensure the accuracy of the radius to ±0.1 μm. The flow domain was partitioned into three sectors (Fig. 6, sector ①, ②, and ③), which were discretized using a mapped mesh of quadrilateral elements. The arrow orientation on the boundaries define the direction of refinement of the meshing. The number of elements and element ratios are specified in Table 2. The element size was changed in a linear fashion along the boundaries. Linear polynomials were used for pressure and velocity components. As the flow inlet boundary condition, a mass flowrate was prescribed at boundary Ⓐ and a static pressure outlet at boundary Ⓔ. The velocity slip condition specified in Eq. (3) was used at the bounding walls Ⓑ, Ⓒ and Ⓓ, Ⓕ being the symmetry axis of the flow. For the diverging flow direction, a negative mass flow was defined at boundary Ⓐ. The numerical solution provides the static pressure loss, calculated from the face-averaged pressures on the boundaries Ⓐand Ⓔ, at a certain prescribed mass flowrate.

To reach the meshing parameters presented in Table 2, a grid independence study was performed. The relative error of the pressure drop was used as a measure to quantify the mesh quality as

$$\varepsilon_p = \left| \frac{\Delta p - \Delta p_{finest}}{\Delta p_{finest}} \right|, \quad (5)$$

with Δp_{finest} being the pressure drop of the finest adopted mesh with 312,000 elements. The chosen mesh of 175,500 elements has shown a relative error $\varepsilon_p \le 0.5\%$ for the smallest and largest pressures

Table 1
Coefficient values of polynomials.

Coefficient	Value	Coefficient	Value
a_0	214.6 μm	a_8	7.9951323e−19 μm^{-7}
a_1	−0.26182	a_9	−3.6614107e−22 μm^{-8}
a_2	1.02455e−3 μm^{-1}	a_{10}	7.150218e−26 μm^{-9}
a_3	−1.307609 μm^{-2}	b_0	476.7 μm
a_4	8.604077e−8 μm^{-3}	b_1	−0.73548
a_5	−3.1809904e−10 μm^{-4}	b_2	4.5015e−4 μm^{-1}
a_6	7.0719917e−13 μm^{-5}	b_4	−7.943e−08 μm^{-2}
a_7	−9.6790273e−16 μm^{-6}		

Table 2
Meshing information at the boundaries.

Boundary	Ⓐ	Ⓑ	Ⓒ	Ⓓ
Number of elements	30	450	240	600
Element size ratio	10	10	5	5

Table 3
Maximum velocity and Mach numbers of a selection of simulation cases.

p_1 [Pa]	p_2 [Pa]	$\dot{m}$ [kg/s]	u_{max} [m/s]	Ma_{max} [-]
3211.0	2394.8	5.16e−10	46.9	0.135
8158.4	7144.8	1.41e−9	49.7	0.143
13159.0	12145.0	2.16e−9	47.4	0.136
2128.3	3003.4	−5.26e−10	45.6	0.131
6697.0	7753.4	−1.39e−9	49.5	0.142
11828.0	12753.0	−1.93e−9	42.4	0.122

investigated regardless of the flow direction. The solution of the fully compressible Navier–Stokes-Fourier equations showed negligible local compressibility effects. The maximum absolute velocities (u_{max}) and Mach numbers (Ma) are present in the nozzle region for all investigated mean pressure levels and are specified in Table 3 for a selection of simulation cases. As visible, the Mach number does not exceed 0.15 for any of the simulation cases. Additionally the obtained temperature fields do not show relevant deviation ($dT/T_0 \leq 0.1\%$) from the ambient temperature T_0, which was applied as boundary condition.

As can be readily seen by analyzing the velocity fields obtained via CFD (Fig. 7), performing flow simulations via two-dimensional modeling was of crucial importance, owing to the strong and sudden changes in radius along the channel structure. Even if the flow is indeed of a two-dimensional nature, the radial velocity is non-zero only in the close proximity of the nozzle of the tapered channel (Fig. 7a). This holds true for all conducted simulations. A zoom on this region of interest is presented for four simulation cases corresponding to $Kn_m = 0.1$ (Fig. 7b/d) and $Kn_m = 0.03$ (Fig. 7c/e) in converging and diverging directions, showcasing the radial velocity distribution and streamlines of the flow. The presented simulation cases are limited to rarefaction levels in the slip-flow regime, owing to the modeling approach used.

For the converging flow direction (Fig. 7b/c), a region of high radial velocity is located at the outlet of the nozzle, with peak velocities of around 11 m/s. The sudden expansion at the exit of the nozzle causes a recirculation zone. All simulated flow cases have similar peak velocities (see Table 3) but different densities, owing to the different mean pressures. For equal velocities, higher density flows correspond to higher mass flow rates, thus higher flow inertia, which creates a larger recirculation zone during the expansion of the flow. This is a well-known behavior in pure continuum flows, too [54]. The diverging flow direction (Fig. 7d/e) shows a similar high radial velocity at the entrance and exit of the nozzle. The recirculation zone for the diverging flow does not show the same prominence in the change of size as a function of mean pressure. However, in contrast to the converging flow direction, the size of the recirculation zone decreases with higher mean pressure. In this case the higher inertia flow (higher mean pressure and higher mean density) slightly compresses the recirculation zone, leading to a reduction in its size.

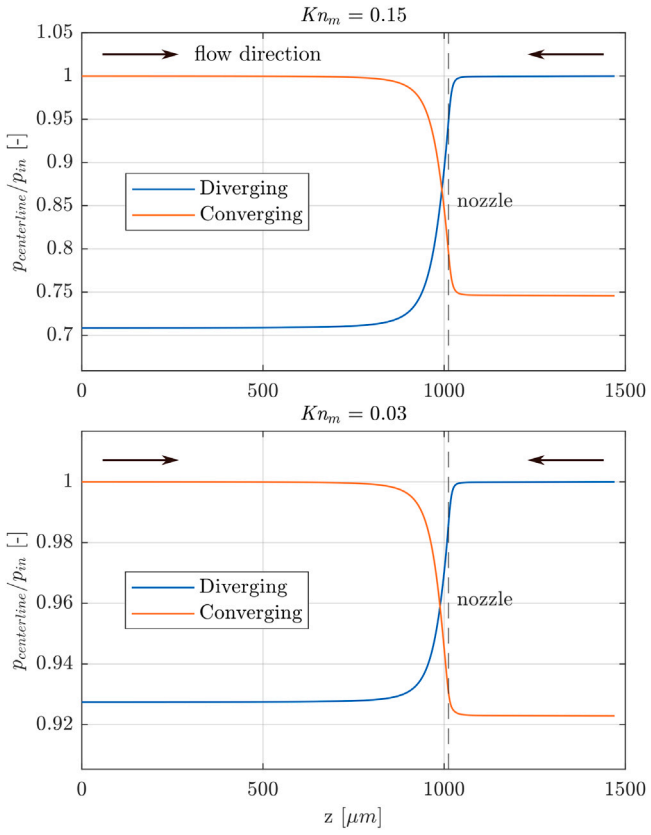

Fig. 8. Numerical centerline pressures in both flow directions, and for two different levels of rarefaction.

Via this preliminary analysis, it is possible to argue that the size of the recirculation zones are dependent prevalently on the Reynolds number and are only weakly affected by the rarefaction of the flow. The localized high radial velocity is connected to the main static pressure loss in the flow. Fig. 8 presents the corresponding centerline pressure $p_{centerline}$ normalized by the inlet pressure p_{in} for the flow cases with the highest and lowest rarefaction. Let us note here that owing to the low density in the flow, the local difference of static and total pressures is negligible. For both rarefaction levels and flow directions, the static pressure loss is localized at the smallest radius, corresponding to the nozzle of the tapered channel. The linear pressure loss in the section far from the nozzle in the tapered channel ($z \leq 800$ μm) and in the orifice ($z \geq 1050$ μm) in the aluminum substrate is negligible compared to the overall pressure loss. This enforces the need for high precision dimensional characterization of the nozzle region.

It is important to emphasize here, that original 3D structures create a real novel demand for 2D and 3D modeling of rarefied flows in complex geometries via kinetic tools. Kinetic databases in the literature are available for long-tubes of varying radius (1D model) or short tubes with constant cross-section. With the existing kinetic databases, it is not possible to model complex flows, as in the tapered channel coupled to a sudden change in cross-section configuration which is presented in this work.

5. Comparison of experimental and numerical results

In order to compare experimental and numerical results we refer to conductance C, which is a typical parameter used in the vacuum community. This parameter is used to quantify the flow characteristics of a pneumatic element and can be calculated as a function of the mass

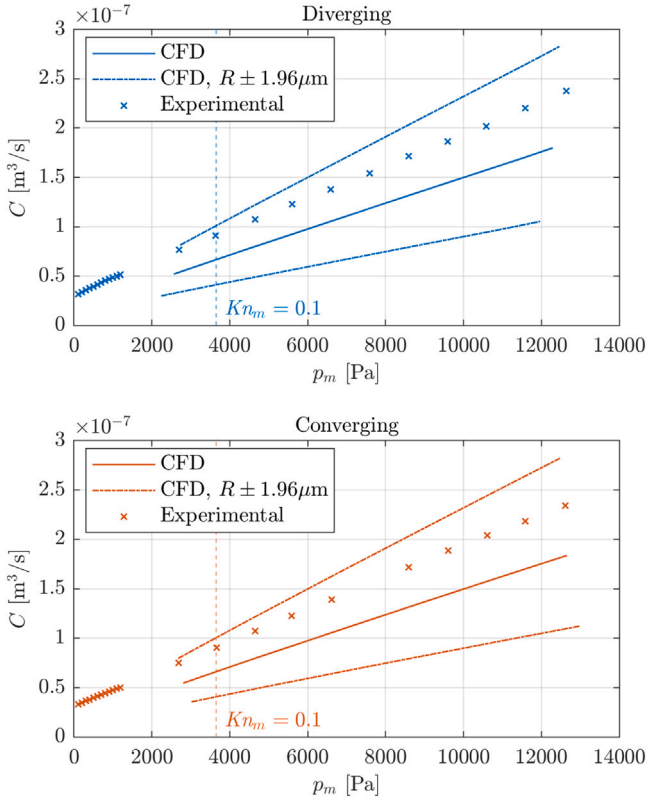

Fig. 9. Experimental and numerical conductance results for converging and diverging flow directions for different mean pressures.

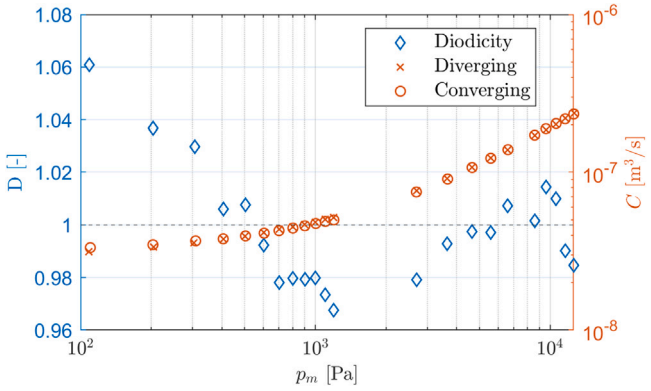

Fig. 10. Experimental conductances in the diverging and converging flow directions, and diodicity, as a function of the mean pressure.

flowrate $\dot{m}$ and the pressure difference $p_1 - p_2$ between the inlet and the outlet

$$C = R_g T \left| \frac{\dot{m}}{p_1 - p_2} \right|. \tag{6}$$

The conductance of the channel structure was measured experimentally for a wide range of mean pressures, from 0.1 kPa to 12.5 kPa, characterizing the channel in the transition, slip, and hydrodynamic regimes. However, the numerical results were obtained only in the slip and hydrodynamic regimes, due to limitations of the modeling tool used. The conductance results were obtained for converging and diverging flow directions as a function of the mean pressure. The experimental and numerical conductance results for both tested flow directions are presented in Fig. 9. The numeric values of the exact pressure conditions and conductance values can be found in Table A.1 (Appendix).

The experimental measurements show a monotonic increase in conductance with increasing mean pressure p_m in the whole investigated range. However, the numerical results for the investigated geometry are slightly lower for both the convergent and divergent flow directions, over the whole range of mean pressure analyzed. To showcase the sensitivity of the numerical results to the radius function along the channel structure, CFD results are also presented for the uncertainty bounds of the radius measurement, that is $R \pm 1.96$ µm (Section 3). The sensitivity of the conductance results to changes in the radius can be seen in the difference of conductance values for the upper and lower radius bounds. A reduction or increase of the radius by just 1.96 µm causes a change in the conductance values of roughly 40%. It is thus important to note that the experimental results are within the uncertainty range of the measured geometry. It is interesting to point out that the upper bounds of the CFD simulations show better agreement with the experimental measurements, suggesting cross-sections with slightly larger radii than the measured ones.

The agreement within uncertainty clearly demonstrates that the TPP fabrication method is suitable for applications in rarefied and non rarefied environments. Furthermore, this agreement also implies a sufficient stability of the sample, as the experiments were conducted during a long experimental campaign. Nevertheless, it is necessary to point out that, to realize experimental vs. numerical comparisons in complex geometries, it is of great importance to have a high precision dimensional characterization of the sample.

As previously mentioned, the flow was modeled via the Navier–Stokes-Fourier equations with modified boundary conditions. Thus, the validity of the numerical results is limited to the hydrodynamic regime and slightly rarefied flows. These models are considered to be valid for $Kn \leq 0.1$. To identify the onset of the transitional flow regime the maximum Knudsen number, $Kn_m = 0.1$, is marked with a vertical dotted line in Fig. 9. As can be seen, this $Kn_m = 0.1$ value corresponds to mean pressure values of roughly $p_m = 3650$ Pa. The trend of the CFD results is continuous even at $p_m \leq 3650$ Pa. There is no visible increase of deviation or change of trend at low mean pressures corresponding to the transitional flow regime. This behavior can be explained by a limited influence of the modeling error on the overall flow behavior.

A direct comparison of diverging and converging flow directions is presented via the diodicity parameter D obtained from the experimental conductances in each direction as

$$D = \frac{C_{conv}}{C_{div}}, \tag{7}$$

C_{conv} and C_{div} being the conductances in the converging and diverging flow direction, respectively.

Neither the numerical nor the experimental results show a significant difference of conductance for the different flow directions, therefore, the diodicity parameter indicates no clear trend regarding a dominant flow direction (Fig. 10). At high rarefaction levels ($p_m \leq 400$ Pa), corresponding to the transitional flow regime, diodicity values of up to 1.06 are measured, while for higher pressure values, the inverse trend is registered with values down to 0.97. The absence of a clear diodicity trend as reported in [7] could be explained by a counter diodicity due to the radius jump from polymer to metal structure. The diodicity of sudden expansions and contractions in 2D flows in the slip flow regime was numerically investigated in [55] using the Lattice-Boltzmann method. Both [7,55] report similar orders of magnitude for diodicity. These rivaling diodicity effects could explain the absence of a clear trend of diodicity in the measured data.

6. Conclusion and perspectives

This paper presents, for the first time in the literature, a 3D microchannel structure suitable for rarefied gas flows exhibiting high-aspect

Table A.1
Experimental C_{exp} and numerical C_{num} conductance values.

Converging					Diverging				
Kn_m [-]	p_{in} [Pa]	p_{out} [Pa]	C_{exp} [m^3/s]	C_{num} [m^3/s]	Kn_m [-]	p_{in} [Pa]	p_{out} [Pa]	C_{exp} [m^3/s]	C_{num} [m^3/s]
3.456	210	10	3.33E−08		3.514	206	10	3.14E−08	
1.870	303	103	3.47E−08		1.860	304	104	3.35E−08	
1.230	409	209	3.68E−08		1.253	401	205	3.57E−08	
0.938	505	305	3.79E−08		0.938	505	305	3.77E−08	
0.754	604	404	3.95E−08		0.756	600	406	3.92E−08	
0.628	705	505	4.11E−08		0.631	700	505	4.14E−08	
0.543	800	600	4.27E−08		0.541	802	602	4.36E−08	
0.474	902	702	4.43E−08		0.474	901	704	4.52E−08	
0.421	1002	802	4.58E−08		0.422	1000	803	4.68E−08	
0.378	1104	904	4.74E−08		0.380	1097	903	4.83E−08	
0.345	1202	1002	4.88E−08		0.346	1198	1002	5.02E−08	
0.317	1299	1099	4.99E−08		0.317	1297	1101	5.16E−08	
0.141	2992	2395	7.49E−08	5.28E−08	0.141	3003	2403	7.65E−08	5.39E−08
0.104	4009	3309	9.05E−08	6.62E−08	0.104	3988	3290	9.12E−08	6.65E−08
0.082	5003	4303	1.07E−07	7.97E−08	0.082	4999	4299	1.07E−07	8.00E−08
0.068	5987	5190	1.23E−07	9.20E−08	0.068	5996	5196	1.23E−07	9.24E−08
0.057	7006	6225	1.39E−07	1.06E−07	0.058	6992	6199	1.38E−07	1.06E−07
0.044	8996	8195	1.72E−07	1.32E−07	0.050	7989	7189	1.54E−07	1.19E−07
0.040	10 003	9203	1.89E−07	1.45E−07	0.044	9000	8200	1.71E−07	1.32E−07
0.036	11 007	10 207	2.04E−07	1.58E−07	0.040	9995	9195	1.86E−07	1.45E−07
0.033	11 990	11 192	2.18E−07	1.70E−07	0.036	10 984	10 184	2.02E−07	1.57E−07
0.030	13 012	12 212	2.34E−07	1.83E−07	0.033	11 984	11 192	2.20E−07	1.70E−07
					0.030	12 991	12 292	2.38E−07	1.84E−07

ratio, and which was advantageously manufactured via two-photon-polymerization. More specifically, a tapered micro-tube of length $L = 1012$ μm with radius varying between 215 μm and 14 μm was printed over an aluminum substrate. The fabricated structure was characterized using a μ-tomograph with a volumetric resolution of $dx = dy = dz = 2.77$ μm, yielding the internal radius distribution. The conductance of the micro-tube was experimentally determined over a wide range of rarefaction levels corresponding to the slip, transitional, and hydrodynamic regimes. The constant volume technique was used for the experimental investigation. Utilizing the measured radius function and velocity slip boundary conditions, the flow was modeled using a CFD approach in the slip and hydrodynamic flow regimes. The experimental results match the numerical results within the uncertainties on the measured geometrical profiles of the tapered channel.

This work has demonstrated the ability to fabricate precise 3D structures in the micro-scale by TPP, by presenting the first experimental investigation of rarefied flow in a circular cross-section micro-tube with varying radius. The experimental and numerical analysis of the flow behavior indicated a leak-proof interface to the metal substrate and stability of the polymer in rarefied gas environments.

These results pave the way for further developments in the field of rarefied gas dynamics in terms of 3D devices with possible channel dimensions close to 10 μm, and very high L/R aspect ratios. The possibility of depositing the fabricated polymer over metal, silicon, or glass substrates, makes the experimental investigations easier and more rapid to handle.

Furthermore, TPP introduces polymers as a viable option for the manufacturing of rarefied gas flow devices. The low thermal conductivity of these polymers is especially desirable for the investigation of temperature-driven rarefied flows, making it possible to manufacture interesting devices such as Knudsen micropumps. It is important to note that low thermal conductivity materials allow a significant reduction in the heating power needed to maintain temperature gradients in the structure.

As a rapid prototyping process, TPP promises to enable faster iterations of designs, thereby enabling the accelerated development of microfluidic devices for rarefied gas flows. The wide range of possible channel geometries opens up the possibility to experimentally investigate alternative cross-sections [56–58] or channels with sudden contractions or expansions [55]. We emphasize here again that original 3D structures create a novel and real demand for 2D and 3D modeling of rarefied flows in complex geometries, using kinetic tools. Literature kinetic databases are available for long-tubes of varying radius (1D model) or short tubes with constant cross-section. With the existing kinetic databases, it is not possible to model complex flows, such as a configuration containing a tapered channel coupled to a sudden change in cross-section, as is presented in this work. Thus, this new fabrication technique offers the possibility to create new benchmark geometries to test and validate 2D and 3D kinetic models.

It can thus be argued that, thanks to this novel fabrication technique, creativity is now more than ever the only limit when it comes to designing next-generation 3D micro-scale devices for gas flows applications, typically in the vacuum, aerospace, health and environment scientific domains.

Future work relates to developing the integration of electronics into such TPP structures. This will allow us to manufacture innovative microsystems with autonomous thermal management and instrumentation for mass transport and sensing purposes.

CRediT authorship contribution statement

Franz Schweizer: Writing – review & editing, Writing – original draft, Methodology, Investigation, Formal analysis, Data curation, Conceptualization. **Klaus Bade:** Resources, Methodology, Investigation. **Lucien Baldas:** Writing – review & editing, Validation, Supervision, Project administration. **Samuel Bergdolt:** Resources, Methodology, Investigation. **Stéphane Colin:** Writing – review & editing, Validation. **Celine Deutschbein:** Resources, Methodology, Investigation. **Stefan Hengsbach:** Resources, Methodology, Investigation. **Jan G. Korvink:** Writing – review & editing, Supervision, Resources, Project administration. **Marcos Rojas-Cárdenas:** Writing – review & editing, Visualization, Validation, Supervision, Resources, Project administration, Methodology, Investigation, Funding acquisition, Formal analysis, Data curation, Conceptualization. **Jürgen J. Brandner:** Writing – review & editing, Validation, Supervision, Resources, Project administration, Methodology, Investigation, Funding acquisition.

Declaration of competing interest

The authors declare that they have no known competing financial interests or personal relationships that could have appeared to influence the work reported in this paper.

Acknowledgments

This work was carried out with the support of the Région Occitanie Pyrénées Méditerranée under the agreement no 00138088/22009727 (ProtOtype de Micro Pompe Knudsen à HYdrogène -HOMER), the Karlsruhe Nano Micro Facility (KNMFi,www.knmf.kit.edu), a Helmholtz Research Infrastructure at Karlsruhe Institute of Technology (KIT, www.kit.edu) and the Deutsche Forschungsgemeinschaft (DFG), Germany for funding the CRC 1527 "HyPERiON" The collaboration between ICA and KNMFi was realized under a long term grant agreement "2022-027-031254" and a short term grant agreement "2020-024-029397". The Research Federation FERMaT (FR 3089) is acknowledged for access to its X-ray tomograph. Finally, we warmly thank Dr. Paul Duru, from the Institut de Mécanique des Fluides de Toulouse (IMFT), Université de Toulouse, CNRS, for the tomography image acquisitions.

Appendix. Experimental and numerical conductance results

See Table A.1.

Data availability

Data will be made available on request.

References

[1] C. Yamarthy, K. Pharas, A. Schultz, S. McNamara, Pneumatic pumping of liquids using thermal transpiration for lab-on-a-chip applications, in: 2009 IEEE Sensors, IEEE, Christchurch, New Zealand, 2009, pp. 1931–1934, URL http://ieeexplore.ieee.org/document/5398354/.

[2] T. Byambadorj, Q. Cheng, Y. Qin, Y.B. Gianchandani, A monolithic Si-micromachined four-stage Knudsen pump for μ GC applications, J. Micromech. Microeng. 31 (3) (2021) 034001, URL https://iopscience.iop.org/article/10.1088/1361-6439/abd264.

[3] J. Jang, S. Wereley, A capacitive micro gas flow sensor based on slip flow, in: 17th IEEE International Conference on Micro Electro Mechanical Systems. Maastricht MEMS 2004 Technical Digest, IEEE, Maastricht, Netherlands, 2004, pp. 540–543, URL http://ieeexplore.ieee.org/document/1290641/.

[4] S. Nakaye, H. Sugimoto, Demonstration of a gas separator composed of Knudsen pumps, Vacuum 125 (2016) 154–164, URL https://linkinghub.elsevier.com/retrieve/pii/S0042207X15301536.

[5] S. Colin, Single-phase gas flow in microchannels, in: Heat Transfer and Fluid Flow in Minichannels and Microchannels, Elsevier, 2014, pp. 11–102, URL https://linkinghub.elsevier.com/retrieve/pii/B9780080983462000028.

[6] R. Brancher, M.V. Johansson, P. Perrier, I. Graur, Measurements of pressure gradient and temperature gradient driven flows in a rectangular channel, J. Fluid Mech. 923 (2021) A35, URL https://www.cambridge.org/core/product/identifier/S0022112021005863/type/journal_article.

[7] I. Graur, T. Veltzke, J.G. Méolans, M.T. Ho, J. Thöming, The gas flow diode effect: theoretical and experimental analysis of moderately rarefied gas flows through a microchannel with varying cross section, Microfluid. Nanofluidics 18 (3) (2015) 391–402, URL http://link.springer.com/10.1007/s10404-014-1445-4.

[8] N. Gaignebet, M. Rojas-Cárdenas, S. Colin, S. Raffy, M. Raison, É. Palleau, Cost and time-efficient microdevice fabrication process for rarefied gas flow applications, Phys. Fluids 36 (12) (2024) 121707, URL https://pubs.aip.org/pof/article/36/12/121707/3325490/Cost-and-time-efficient-microdevice-fabrication.

[9] H.S. Singh, P.M.V. Subbarao, S. Dhanekar, Experimental and numerical study of gas flow through microchannel with 90% bends, J. Micromech. Microeng. 32 (9) (2022) 095003, URL https://iopscience.iop.org/article/10.1088/1361-6439/ac7b0d.

[10] V. Varade, A. Agrawal, A.M. Pradeep, Slip flow through a converging microchannel: experiments and 3D simulations, J. Micromech. Microeng. 25 (2) (2015) 025015, URL https://iopscience.iop.org/article/10.1088/0960-1317/25/2/025015.

[11] I.A. Graur, P. Perrier, W. Ghozlani, J.G. Méolans, Measurements of tangential momentum accommodation coefficient for various gases in plane microchannel, Phys. Fluids 21 (10) (2009) 102004, URL https://pubs.aip.org/pof/article/21/10/102004/256661/Measurements-of-tangential-momentum-accommodation.

[12] P. Perrier, M. Hadj-Nacer, J.G. Méolans, I. Graur, Measurements and modeling of the gas flow in a microchannel: influence of aspect ratios, surface nature, and roughnesses, Microfluid. Nanofluidics 23 (8) (2019) 97, URL http://link.springer.com/10.1007/s10404-019-2259-1.

[13] M. Bergoglio, D. Mari, J. Chen, H. Si Hadj Mohand, S. Colin, C. Barrot, Experimental and computational study of gas flow delivered by a rectangular microchannels leak, Measurement 73 (2015) 551–562, URL https://linkinghub.elsevier.com/retrieve/pii/S0263224115003255.

[14] J.M. Anderson, M.W. Moorman, J.R. Brown, J.M. Hochrein, S.M. Thornberg, K.E. Achyuthan, M.A. Gallis, J.R. Torczynski, T. Khraishi, R.P. Manginell, Isothermal mass flow measurements in microfabricated rectangular channels over a very wide Knudsen range, J. Micromech. Microeng. 24 (5) (2014) 055013, URL https://iopscience.iop.org/article/10.1088/0960-1317/24/5/055013.

[15] K. Srinivasan, P.M. Subbarao, S.R. Kale, Studies on gas flow through smooth microchannel surface – fabrication, characterization, analysis, and tangential momentum accommodation coefficient comparison, Heat Transf. Eng. 41 (6–7) (2020) 607–621, URL https://www.tandfonline.com/doi/full/10.1080/01457632.2018.1546952.

[16] W.H. Fissell, A.T. Conlisk, S. Datta, J.M. Magistrelli, J.T. Glass, A.J. Fleischman, S. Roy, High Knudsen number fluid flow at near-standard temperature and pressure conditions using precision nanochannels, Microfluid. Nanofluidics 10 (2) (2011) 425–433, URL http://link.springer.com/10.1007/s10404-010-0682-4.

[17] E. Arkilic, M. Schmidt, K. Breuer, Gaseous slip flow in long microchannels, J. Microelectromech. Syst. 6 (2) (1997) 167–178, URL http://ieeexplore.ieee.org/document/585795/.

[18] E. Silva, C.J. Deschamps, M. Rojas-Cárdenas, C. Barrot-Lattes, L. Baldas, S. Colin, A time-dependent method for the measurement of mass flow rate of gases in microchannels, Int. J. Heat Mass Transfer 120 (2018) 422–434, URL https://linkinghub.elsevier.com/retrieve/pii/S0017931017332416.

[19] M. Hadj Nacer, I. Graur, P. Perrier, J.G. Méolans, M. Wuest, Gas flow through microtubes with different internal surface coatings, J. Vac. Sci. Technol. A: Vac. Surfaces Films 32 (2) (2014) 021601, URL https://pubs.aip.org/jva/article/32/2/021601/985353/Gas-flow-through-microtubes-with-different.

[20] L. Marino, Experiments on rarefied gas flows through tubes, Microfluid. Nanofluidics 6 (1) (2009) 109–119, URL http://link.springer.com/10.1007/s10404-008-0311-7.

[21] P. Perrier, I.A. Graur, T. Ewart, J.G. Méolans, Mass flow rate measurements in microtubes: From hydrodynamic to near free molecular regime, Phys. Fluids 23 (4) (2011) 042004, URL https://pubs.aip.org/pof/article/23/4/042004/933056/Mass-flow-rate-measurements-in-microtubes-From.

[22] H. Yamaguchi, T. Hanawa, O. Yamamoto, Y. Matsuda, Y. Egami, T. Niimi, Experimental measurement on tangential momentum accommodation coefficient in a single microtube, Microfluid. Nanofluidics 11 (1) (2011) 57–64, URL http://link.springer.com/10.1007/s10404-011-0773-x.

[23] T. Ewart, P. Perrier, I. Graur, J.G. Méolans, Tangential momemtum accommodation in microtube, Microfluid. Nanofluidics 3 (6) (2007) 689–695, URL http://link.springer.com/10.1007/s10404-007-0158-3.

[24] S.E. Vargo, Initial results from the first MEMS fabricated thermal transpiration-driven vacuum pump, in: AIP Conference Proceedings, Vol. 585, AIP, Sydney (Australia), 2001, pp. 502–509, URL https://pubs.aip.org/aip/acp/article/585/1/502-509/577773. ISSN: 0094243X.

[25] N.K. Gupta, Y.B. Gianchandani, A planar cascading architecture for a ceramic Knudsen micropump, in: TRANSDUCERS 2009 - 2009 International Solid-State Sensors, Actuators and Microsystems Conference, IEEE, Denver, CO, USA, 2009, pp. 2298–2301, URL http://ieeexplore.ieee.org/document/5285895/.

[26] N.K. Gupta, Y.B. Gianchandani, Thermal transpiration in mixed cellulose ester membranes: Enabling miniature, motionless gas pumps, Microporous Mesoporous Mater. 142 (2–3) (2011) 535–541, URL https://linkinghub.elsevier.com/retrieve/pii/S1387181110004750.

[27] Z. Wang, X. Yan, Q. Zhou, Q. Wang, D. Zhao, H. Wu, A directly moldable, highly compact, and easy-for-integration 3D micromixer with extraordinary mixing performance, Anal. Chem. 95 (23) (2023) 8850–8858, URL https://pubs.acs.org/doi/10.1021/acs.analchem.3c00335.

[28] F. Perrucci, V. Bertana, S. Marasso, G. Scordo, S. Ferrero, C. Pirri, M. Cocuzza, A. El-Tamer, U. Hinze, B. Chichkov, G. Canavese, L. Scaltrito, Optimization of a suspended two photon polymerized microfluidic filtration system, Microelectron. Eng. 195 (2018) 95–100, URL https://linkinghub.elsevier.com/retrieve/pii/S016793171830145X.

[29] Y. Zhou, H. Wang, Z. Ma, J.K.W. Yang, Y. Ai, Acoustic vibration-induced actuation of multiple microrotors in microfluidics, Adv. Mater. Technol. 5 (9) (2020) 2000323, URL https://onlinelibrary.wiley.com/doi/10.1002/admt.202000323.

[30] Y. Lin, Y. Gao, M. Wu, R. Zhou, D. Chung, G. Caraveo, J. Xu, Acoustofluidic stick-and-play micropump built on foil for single-cell trapping, Lab A Chip 19 (18) (2019) 3045–3053, URL http://xlink.rsc.org/?DOI=C9LC00484J.

[31] D. Zhang, G. López-Quesada, S. Bergdolt, S. Hengsbach, K. Bade, S. Colin, M. Rojas-Cárdenas, 3D micro-structures for rarefied gas flow applications manufactured via two-photon-polymerization, Vacuum 211 (2023) 111915, URL https://linkinghub.elsevier.com/retrieve/pii/S0042207X23001124.

[32] A. Alexeenko, S. Gimelshein, D. Levin, R. Collins, Numerical modeling of axisymmetric and three-dimensional flows in MEMS nozzles, in: 36th AIAA/ASME/SAE/ASEE Joint Propulsion Conference and Exhibit, American Institute of Aeronautics and Astronautics, Las Vegas,NV,U.S.A., 2000, URL https://arc.aiaa.org/doi/10.2514/6.2000-3668.

[33] G. López Quesada, G. Tatsios, D. Valougeorgis, M. Rojas-Cárdenas, L. Baldas, C. Barrot, S. Colin, Thermally driven pumps and diodes in multistage assemblies consisting of microchannels with converging, diverging and uniform rectangular cross sections, Microfluid. Nanofluidics 24 (7) (2020) 54, URL https://link.springer.com/10.1007/s10404-020-02357-z.

[34] F. Sharipov, G. Bertoldo, Rarefied gas flow through a long tube of variable radius, J. Vac. Sci. Technol. A: Vac. Surfaces Films 23 (3) (2005) 531–533, URL https://pubs.aip.org/jva/article/23/3/531/391427/Rarefied-gas-flow-through-a-long-tube-of-variable.

[35] I. Graur, M. Ho, Rarefied gas flow through a long rectangular channel of variable cross section, Vacuum 101 (2014) 328–332, URL https://linkinghub.elsevier.com/retrieve/pii/S0042207X1300331X.

[36] V. Titarev, E. Shakhov, S. Utyuzhnikov, Rarefied gas flow through a diverging conical pipe into vacuum, Vacuum 101 (2014) 10–17, URL https://linkinghub.elsevier.com/retrieve/pii/S0042207X13002479.

[37] O. Sazhin, A. Sazhin, Rarefied gas flow into vacuum through linearly diverging and converging channels, Int. J. Heat Mass Transfer 203 (2023) 123842, URL https://linkinghub.elsevier.com/retrieve/pii/S0017931022013102.

[38] C. Tantos, F. Litovoli, T. Teichmann, I. Sarris, C. Day, Numerical study of rarefied gas flow in diverging channels of finite length at various pressure ratios, Fluids 9 (3) (2024) 78, URL https://www.mdpi.com/2311-5521/9/3/78.

[39] A. Ebrahimi, V. Shahabi, E. Roohi, Pressure-driven nitrogen flow in divergent microchannels with isothermal walls, Appl. Sci. 11 (8) (2021) 3602, URL https://www.mdpi.com/2076-3417/11/8/3602.

[40] A. Ebrahimi, E. Roohi, DSMC investigation of rarefied gas flow through diverging micro- and nanochannels, Microfluid. Nanofluidics 21 (2) (2017) 18, URL http://link.springer.com/10.1007/s10404-017-1855-1.

[41] K.-S. Lee, D.-Y. Yang, S.H. Park, R.H. Kim, Recent developments in the use of two-photon polymerization in precise 2D and 3D microfabrications, Polym. Adv. Technol. 17 (2) (2006) 72–82, URL https://onlinelibrary.wiley.com/doi/10.1002/pat.664.

[42] J. Fischer, M. Wegener, Three-dimensional optical laser lithography beyond the diffraction limit, Laser Photonics Rev. 7 (1) (2013) 22–44, URL https://onlinelibrary.wiley.com/doi/10.1002/lpor.201100046.

[43] X. Zhou, Y. Hou, J. Lin, A review on the processing accuracy of two-photon polymerization, AIP Adv. 5 (3) (2015) 030701, URL https://pubs.aip.org/adv/article/5/3/030701/279889/A-review-on-the-processing-accuracy-of-two-photon.

[44] M. Rojas-Cárdenas, E. Silva, M.-T. Ho, C.J. Deschamps, I. Graur, Time-dependent methodology for non-stationary mass flow rate measurements in a long microtube: Experimental and numerical analysis at arbitrary rarefaction conditions, Microfluid. Nanofluidics 21 (5) (2017) 86, URL http://link.springer.com/10.1007/s10404-017-1920-9.

[45] M. Rojas-Cárdenas, I. Graur, P. Perrier, J.G. Méolans, A new method to measure the thermal slip coefficient, Int. J. Heat Mass Transfer 88 (2015) 766–774, URL https://linkinghub.elsevier.com/retrieve/pii/S0017931015004901.

[46] E. Silva, M. Rojas-Cardenas, C.J. Deschamps, Experimental analysis of velocity slip at the wall for gas flows of nitrogen, R134a, and R600a through a metallic microtube, Int. J. Refrig. 66 (2016) 121–132, URL https://linkinghub.elsevier.com/retrieve/pii/S0140700716000384.

[47] A. Maali, S. Colin, B. Bhushan, Slip length measurement of gas flow, Nanotechnology 27 (37) (2016) 374004, URL https://iopscience.iop.org/article/10.1088/0957-4484/27/37/374004.

[48] H. Yamaguchi, M. Rojas-Cárdenas, P. Perrier, I. Graur, T. Niimi, Thermal transpiration flow through a single rectangular channel, J. Fluid Mech. 744 (2014) 169–182, URL https://www.cambridge.org/core/product/identifier/S0022112014000706/type/journal_article.

[49] M. Rojas-Cárdenas, I. Graur, P. Perrier, J.G. Méolans, Time-dependent experimental analysis of a thermal transpiration rarefied gas flow, Phys. Fluids 25 (7) (2013) 072001, URL https://pubs.aip.org/pof/article/25/7/072001/314358/Time-dependent-experimental-analysis-of-a-thermal.

[50] M. Rojas-Cárdenas, I. Graur, P. Perrier, J. Meolans, An experimental and numerical study of the final zero-flow thermal transpiration stage, J. Therm. Sci. Technol. 7 (3) (2012) 437–452, URL https://www.jstage.jst.go.jp/article/jtst/7/3/7_437/_article.

[51] J. Pitakarnnop, S. Varoutis, D. Valougeorgis, S. Geoffroy, L. Baldas, S. Colin, A novel experimental setup for gas microflows, Microfluid. Nanofluidics 8 (1) (2010) 57–72, URL http://link.springer.com/10.1007/s10404-009-0447-0.

[52] D.A. Lockerby, J.M. Reese, D.R. Emerson, R.W. Barber, Velocity boundary condition at solid walls in rarefied gas calculations, Phys. Rev. E 70 (1) (2004) 017303, URL https://link.aps.org/doi/10.1103/PhysRevE.70.017303.

[53] F. Sharipov, Data on the velocity slip and temperature jump on a gas-solid interface, J. Phys. Chem. Ref. Data 40 (2) (2011) 023101, URL https://pubs.aip.org/jpr/article/40/2/023101/242102/Data-on-the-Velocity-Slip-and-Temperature-Jump-on.

[54] L. Chen, K. Asai, T. Nonomura, G. Xi, T. Liu, A review of backward-facing step (BFS) flow mechanisms, heat transfer and control, Therm. Sci. Eng. Prog. 6 (2018) 194–216, URL https://linkinghub.elsevier.com/retrieve/pii/S2451904918300167.

[55] A. Agrawal, L. Djenidi, R.A. Antonia, Simulation of gas flow in microchannels with a sudden expansion or contraction, J. Fluid Mech. 530 (2005) 135–144, URL http://www.journals.cambridge.org/abstract_S0022112005003691.

[56] I. Graur, F. Sharipov, Gas flow through an elliptical tube over the whole range of the gas rarefaction, Eur. J. Mech. B Fluids 27 (3) (2008) 335–345, URL https://linkinghub.elsevier.com/retrieve/pii/S0997754607000660.

[57] I. Graur, F. Sharipov, Non-isothermal flow of rarefied gas through a long pipe with elliptic cross section, Microfluid. Nanofluidics 6 (2) (2009) 267–275, URL http://link.springer.com/10.1007/s10404-008-0325-1.

[58] K. Ritos, Y. Lihnaropoulos, S. Naris, D. Valougeorgis, Pressure- and temperature-driven flow through triangular and trapezoidal microchannels, Heat Transf. Eng. 32 (13–14) (2011) 1101–1107, URL http://www.tandfonline.com/doi/abs/10.1080/01457632.2011.562455.